Fluorapatite as the Primary Rare Earth Element Host in the Hecla-Kilmer Alkaline Carbonatite Deposit, Northern Ontario, Canada: Mineralogical Controls, TIMA-X–Guided Microanalysis, and Implications for Rare Earth Processing

Tassos Grammatikopoulos[1,*], Reagan Glazier[2], Jared Galenzoski[2], Steven Grammatikopoulos[3], Marek Dosbaba[4], Eligiusz P. Gugala[4] and Brian Joy[5]

[1] *SGS Canada Inc., Lakefield, Ontario, Canada*

[2] *Neotech Metals Corp., Vancouver, British Columbia, Canada*

[3] *Department of Chemical Engineering, McGill University, Montreal, Quebec, Canada*

[4] *TESCAN, Libušina třída 863/21, 623 00 Brno, Czech Republic*

[5] *Department of Geological Sciences and Geological Engineering, Queen's University, Kingston, Ontario, Canada*

**Corresponding author: tassos.grammatikopoulos@sgs.com*

Abstract

The Hecla-Kilmer (H-K) deposit, in Northern Ontario, Canada, is a REE-enriched iron oxide–copper–gold (IOCG) style mineralization with well-developed apatite. Drilling has returned intercepts of up to 471 m at 0.7% total rare earth oxide (TREO), of which 20% is magnet rare earth oxide (MREO), together with 0.13% niobium oxide; higher-grade sub-intervals include 361 m at 1.0% TREO and 54 m at 1.06% TREO. Mineralogical characterization of a composite sample reveals a silicate-dominated gangue (biotite/phlogopite, amphiboles, pyroxenes) alongside 11.3% apatite, 6.5% magnetite, and 5.5% calcite. Discrete REE minerals (REM) such as monazite, britholite, synchysite and pyrochlore/columbite make up less than 1% of the mass, far too little to account for the bulk REE grade. Advanced microanalysis (TIMA-X, EPMA, LA-ICP-MS) indicates that the apatite contains unusually high concentrations of TREE (5.9%) and TREE+Y (6.2%). Apatite is therefore the primary host of the REE+Y budget (>80%). At a grind size of P_{80} = 183 µm, liberation of the individual REM is limited (25–50%), so a high-grade REE concentrate is difficult to produce from grains that are both low in grade and finely disseminated. Conversely, apatite is highly liberated (84%). Because the REE and Y substitute directly into the apatite lattice, they cannot be separated from the host mineral by physical means. Preliminary metallurgical testwork nevertheless demonstrates >75% TREO recovery, with the apatite-hosted REE leaching readily in approximately 6 h at 50 °C. Process mineralogy has therefore shifted the strategic focus of the project away from the discrete REM and toward a high-grade, REE-enriched phosphate (apatite) concentrate. Such a product suits established phosphate producers able to recover REE as a byproduct, and reduces overall processing complexity. The Fe-oxides of the deposit offer additional product potential.

Keywords: *rare earth elements; carbonatite; fluorapatite; TIMA-X; automated mineralogy; XRD reconciliation; process mineralogy; critical minerals*

1. Introduction

Rare earth supply vulnerability outside China is a processing problem. China holds roughly 92% of global REE separation and processing capacity, and that concentration has pushed feedstock mineralogy to the front of the discussion: the phase in which a deposit's REE are locked determines whether a Western supply chain can be built around it at all (Chakhmouradian et al., 2017).

Most REE projects target discrete REE minerals. Monazite, bastnasite, synchysite, xenotime and other REM typically occur as fine, disseminated grains sitting inside complex silicate and/or carbonate gangue. Producing a marketable concentrate out of them usually means grinding well below 40–50 µm, running multi-stage flotation or gravity and magnetic circuits, and dealing with the Th and U that travel with the REE.

Rare earth elements (REEs) are integral to various modern technologies due to their unique chemical and physical properties. They typically occur in low concentrations within a multitude of mineralogical environments, often presenting as minor constituents associated with complex gangue mineral assemblages. The inherent complexity of REE mineralogy poses significant challenges for effective processing and recovery.

Successful recovery of REEs relies heavily on detailed mineralogical characterization that elucidates the mineral associations, grain size distributions, and liberation characteristics of REE-bearing phases. Such detailed process mineralogy enables the identification of ores with potential for REE recovery, especially as high-grade resources become depleted and unconventional sources such as low-grade ores and tailings are increasingly targeted. Studies emphasize that the quality of concentrates and the overall recovery efficiency are strongly controlled by the intrinsic ore mineralogy and particle size distribution, as heterogeneities in mineral liberation can lead to antagonistic or synergistic interactions between valuable and gangue minerals during beneficiation (Xu et al., 2020).

The intricate mineralogy also influences the design and implementation of processing flowsheets. For instance, the presence of complex intergrowths and poorly liberated mineral particles requires an optimization of comminution and separation techniques to ensure improved liberation and selective recovery. Process mineralogy, therefore, is not only critical for evaluating the economic feasibility of deposits but is also essential for innovating or improving existing beneficiation methods to meet industrial demand efficiently (Watts and Andersen 2025). Such mineralogical insights are crucial for emerging REE supply chains, particularly given the expanding global demand and the strategic importance of these elements in advanced technologies. Furthermore, tailored beneficiation strategies derived from mineralogical studies can contribute to reducing environmental impacts by minimizing reagent use and maximizing resource efficiency (Özer et al 2025).

Apatite-hosted deposits work on a different principle. REE and Y enter the apatite structure directly, replacing Ca^{2+} on the A-site with charge balance maintained by coupled substitution of Na^{+} or Si^{4+} (Pan & Fleet, 2002; Chakhmouradian et al., 2017; Broom-Fendley et al., 2016). The consequence for processing is direct. The REE are not inclusions and not a separate phase, so there is nothing to liberate. They follow whatever fraction of the ore reports to an apatite concentrate, and they are recovered by attacking the phosphate matrix itself.

This paper reports an integrated process mineralogy study of the H-K deposit using XRD, TIMA-X, EPMA and LA-ICP-MS. The investigation addresses the occurrence of the discrete REM, the deportment of the REE and the resulting metallurgical options. Taken together, the results recast H-K as a phosphate-first critical minerals project in which the primary metallurgical product is a REE-enriched fluorapatite concentrate.

2. Geological Setting

The H-K deposit sits within a Proterozoic alkaline carbonatite intrusive complex in Northern Ontario (Figure 1), about 2.5 hours by maintained road from Timmins and some 15 km from an existing 180 MW hydroelectric facility. Mineralization is REE-enriched iron oxide with well-developed fluorapatite, set in a silicate-dominated assemblage of biotite and phlogopite, amphibole and pyroxene, with calcite, dolomite and magnetite. Diamond drilling has returned intercepts of up to 471 m at 0.7% total rare earth oxide (TREO) with 20% magnet rare earth oxides

(MREO) and 0.13% niobium oxide. Higher-grade sub-intervals include 361 m at 1.0% TREO and 54 m at 1.06% TREO. A maiden mineral resource estimate is in progress. Columbite-group minerals and magnetite are present as additional recoverable phases, and gallium of up to 55 ppm has been confirmed in the fluorapatite fraction.

The architecture is a familiar one for carbonatite complexes, where apatite is a well-documented REE host (Chakhmouradian et al., 2017; Anenburg et al., 2021). It also has a functional parallel outside the igneous realm: the REE-bearing biogenic apatite in deep-sea sediments near Minamitorishima, Japan, is attractive for the same reason H-K is, namely that the REE leach readily from an apatite lattice at low temperature (Kato et al., 2011; Takaya et al., 2018). H-K offers comparable chemistry at surface, with established road access and hydroelectric power nearby.

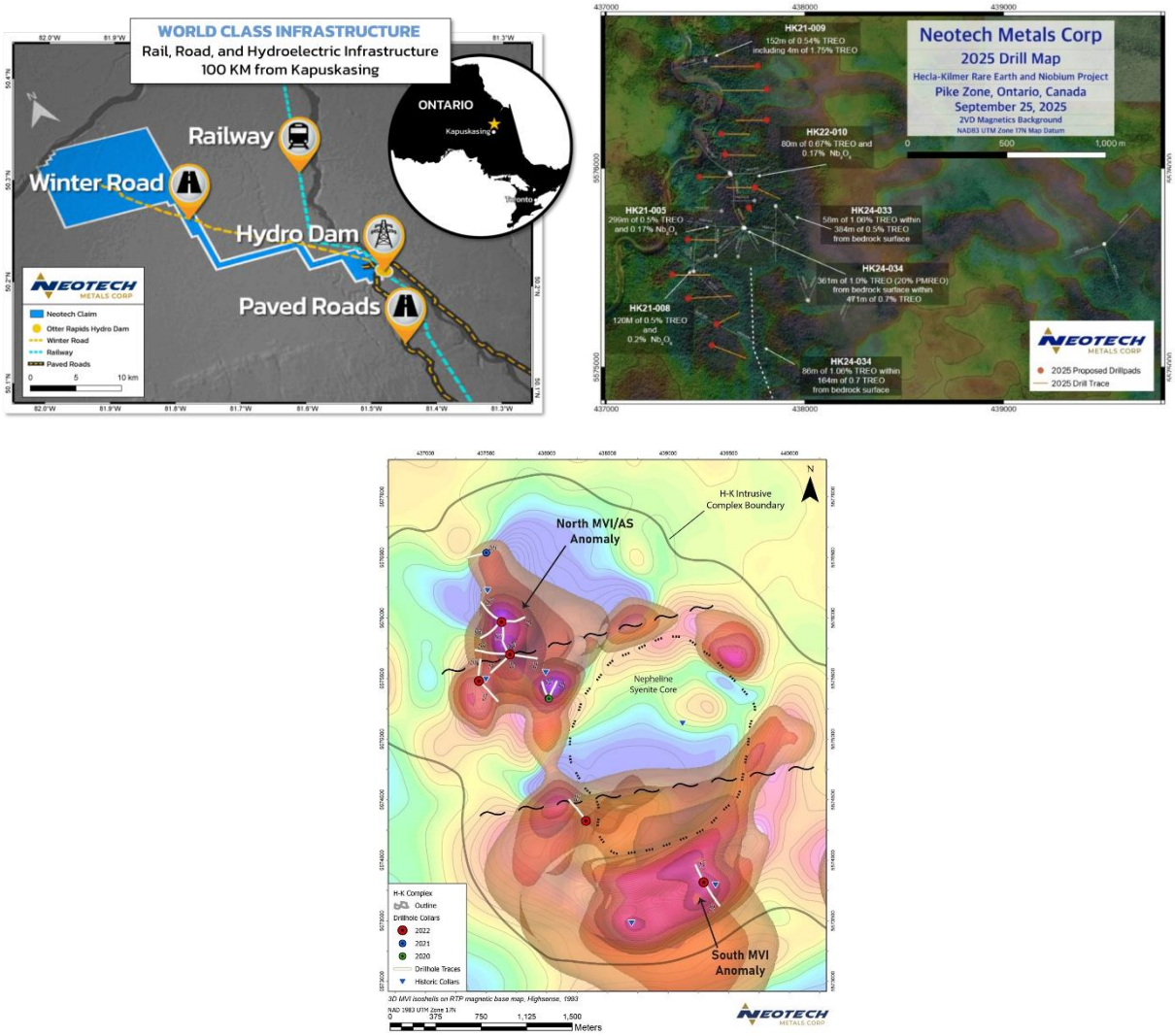

Figure 1. Location of the Hecla-Kilmer alkaline carbonatite complex, Northern Ontario, drilling sites at the Pike Zone of the project and a geologic map showing the zonal anomalies across the Hecla-Kilmer area.

3. Materials and Methods

3.1. Samples and Sample Preparation

One composite (Master Comp –10 Mesh, hereafter "Composite") and eight variability samples (E446054, E446142, E446176, E446246, E446317, D141522, D141577, D141682) representing drill core from across the deposit were submitted to the SGS Advanced Mineralogy Facility, Lakefield, Ontario (Grammatikopoulos, 2026). The Composite was stage-crushed to a P_{80} of approximately 200 µm, screened, and split by mass distribution into four size fractions (+212 µm, –212/+106 µm, –106/+25 µm and –25 µm). Each fraction was analyzed separately and the results recombined arithmetically to a calculated head. The TIMA-X-measured P_{80} of the Composite is 183 µm.

3.2. TIMA-X Automated Mineralogy

Modal mineralogy, grain size, liberation, exposure and mineral association were measured on a TESCAN Integrated Mineral Analyzer (TIMA-X) running software 2.12, following established practice for SEM-based automated mineralogy (Fandrich et al., 2007; Sylvester, 2012; Gugala, 2025). The instrument collects a back-scattered electron (BSE) image and multiple co-registered energy-dispersive X-ray (EDS) maps per field of view. A spectral-summing algorithm raises sensitivity to less-abundant elements without sacrificing acquisition speed. Pixel-level BSE and EDS data are segmented and classified against a project-specific mineral list, producing a digital, mineralogically classified copy of each polished section in which the underlying spectra remain addressable for later reclassification or audit.

This matters for the present study. REE and Y give strong, unambiguous EDS signatures in this assemblage, so a grain classified as fluorapatite, monazite, synchysite, bastnasite, allanite or pyrochlore is identified by its own chemistry rather than by deconvolution of an overlapping diffraction pattern.

4. Results

4.1. Geochemistry and Modal Mineralogy by TIMA-X

The Composite is LREE-enriched. TREE+Y rises from 4,258 g/t in the coarse (+212 µm) fraction to 8,093 g/t in the -106/+25 µm fraction (Table 1), giving a mass-weighted calculated head of 6,866 g/t. Niobium stays below 900 g/t in every fraction and tantalum is below the 20 g/t detection limit throughout, so neither is upgraded by comminution or by size classification. Thorium (124–232 g/t) and uranium (21–36 g/t) are present at levels normal for carbonatite-affiliated systems and are not strongly enriched. That is a favorable starting point for radionuclide management in any downstream concentrate or leachate.

Silicate gangue dominates the Composite (Table 2): biotite and phlogopite together account for 27.1 wt%, amphiboles 13.5 wt% and pyroxenes 11.4 wt%, with magnetite at 6.53 wt% and calcite at 5.45 wt%. Fluorapatite makes up 11.3 wt%, plus a further 0.11 wt% reporting to mixed apatite-silicate composite particles. It is somewhat concentrated in the intermediate fractions, at 12.6 and 14.8 wt% in the -212/+106 µm and -106/+25 µm fractions respectively, against only 5.68 wt% in the coarse fraction.

The discrete REM inventory is the critical observation. Monazite, synchysite, bastnasite, allanite, other REM, pyrochlore and columbite (Ce,La,Ti) together total 0.58 wt% of the Composite. Even assigning them an implausibly

high average REE content, that abundance falls roughly an order of magnitude short of the 6,866 g/t TREE+Y measured in the head (Table 1). The REE budget must therefore be carried elsewhere.

Table 1. Whole-rock geochemistry of the Composite by size fraction, with mass-weighted calculated head.

Element	+212 µm	–212/+106 µm	–106/+25 µm	–25 µm	Calc. head
Mass of fraction (%)	16.9	20.6	31.3	31.2	100
TREE+Y (g/t)	4,258.30	7,626.10	8,092.80	6,545.40	6,866
P2O5 (%)	2.26	4.84	5.63	4.32	4.49
U (g/t)	21.3	30.1	30.2	35.5	30
Th (g/t)	124	215	232	205	199
Nb (g/t)	854	886	891	797	854
Ta (g/t)	<20	<20	<20	<20	<20
Sc (g/t)	<25	<25	<25	<25	<25

Table 2. TIMA-X modal mineralogy of the Composite, calculated head and size fractions (wt%).

Fraction	Combined	+212 um		-212/+106 um		-106/+25 um		-25 um	
Mass % of Size Fraction [%]	100.0	16.9		20.6		31.3		31.2	
	Sample	Sample	Fraction	Sample	Fraction	Sample	Fraction	Sample	Fraction
Monazite	0.05	0.01	0.03	0.01	0.05	0.01	0.04	0.02	0.07
Synchysite	0.36	0.01	0.04	0.02	0.07	0.03	0.08	0.31	0.98
Bastnasite	0.01	0.00	0.00	0.00	0.00	0.00	0.00	0.01	0.02
Allanite	0.01	0.00	0.01	0.00	0.01	0.00	0.01	0.00	0.00
Other REM	0.06	0.01	0.08	0.01	0.06	0.02	0.06	0.02	0.05
Pyrochlore	0.06	0.01	0.06	0.01	0.06	0.02	0.06	0.02	0.07
Columbite(Ce,La,Ti)	0.04	0.01	0.06	0.01	0.05	0.01	0.04	0.01	0.02
Barite	0.01	0.00	0.01	0.00	0.01	0.00	0.01	0.01	0.02
Zircon	0.01	0.00	0.01	0.00	0.01	0.00	0.01	0.00	0.01
Zirconolite	0.02	0.00	0.01	0.01	0.02	0.01	0.02	0.01	0.02
Calcite	5.45	0.62	3.66	1.13	5.49	1.99	6.37	1.71	5.47
Dolomite	0.99	0.18	1.06	0.26	1.24	0.32	1.02	0.23	0.75
Other Carbonates	0.56	0.05	0.31	0.09	0.43	0.14	0.45	0.28	0.88
Witherite	0.05	0.01	0.05	0.01	0.05	0.01	0.04	0.02	0.05
Montmorillonite	0.10	0.02	0.12	0.03	0.13	0.03	0.08	0.02	0.08
Nepheline	2.44	0.80	4.72	0.77	3.71	0.63	2.01	0.24	0.78
Olivine	0.13	0.02	0.13	0.04	0.20	0.04	0.13	0.02	0.08
Pyroxenes	11.4	2.71	16.1	2.83	13.8	3.83	12.2	2.02	6.48
Amphiboles	13.5	3.21	19.0	3.05	14.8	3.09	9.86	4.12	13.2
Quartz	0.83	0.12	0.72	0.16	0.80	0.22	0.69	0.33	1.04
Plagioclase	0.89	0.23	1.35	0.20	0.99	0.21	0.66	0.26	0.82
Orthoclase	0.67	0.09	0.56	0.16	0.79	0.23	0.73	0.19	0.60
Albite	3.15	0.88	5.20	0.84	4.08	0.82	2.61	0.61	1.96
Biotite/Phlogopite	27.1	3.17	18.8	4.21	20.5	9.19	29.4	10.5	33.7
Chlorite	2.37	0.34	1.99	0.44	2.16	0.57	1.81	1.02	3.28
Muscovite	1.40	0.31	1.83	0.36	1.75	0.38	1.22	0.35	1.13
Titanite	0.42	0.09	0.54	0.09	0.45	0.11	0.36	0.12	0.39
Perovskite Group	2.10	0.36	2.13	0.42	2.03	0.51	1.63	0.81	2.61
Other Silicates	0.98	0.24	1.43	0.24	1.16	0.25	0.81	0.24	0.78
Apatite	11.3	0.96	5.68	2.60	12.6	4.64	14.8	3.09	9.89
Apatite/Silicates	0.11	0.02	0.14	0.02	0.12	0.03	0.08	0.04	0.13
Nagelschmidtite	0.11	0.03	0.17	0.03	0.15	0.03	0.09	0.02	0.06
Fluorite	0.79	0.01	0.04	0.02	0.08	0.05	0.15	0.72	2.32
Magnetite	6.53	1.47	8.70	1.58	7.68	2.47	7.88	1.01	3.24
Ilmenorutile	0.02	0.01	0.04	0.01	0.03	0.01	0.02	0.00	0.01
Ilmenite	0.22	0.05	0.29	0.05	0.25	0.08	0.26	0.04	0.13
Rutile	0.11	0.03	0.16	0.03	0.13	0.04	0.12	0.02	0.06
Rutile(Nb)	0.01	0.00	0.01	0.00	0.01	0.00	0.01	0.00	0.01
Pyrite	2.38	0.66	3.88	0.57	2.75	0.74	2.37	0.42	1.33
Pyrrhotite	1.15	0.14	0.82	0.23	1.10	0.42	1.35	0.36	1.16
Other Sulphides	0.04	0.01	0.04	0.01	0.03	0.01	0.03	0.02	0.05
Other	2.16	0.02	0.13	0.05	0.22	0.12	0.39	1.97	6.33
Total	100.0	16.9	100.0	20.6	100.0	31.3	100.0	31.2	100.0

4.2. TIMA-X Mineralogical Assay Reconciliation

TIMA-X mineralogical assays, back-calculated from modal abundances and measured mineral compositions, were compared against direct whole-rock chemical assays for each size fraction. Agreement is close across all reconciled elements (Na, Mg, Al, Si, P, Ca, La, Ce, Nd). Silicon returns 16.0, 14.3, 13.4 and 13.6 wt% by TIMA-X against

16.1, 14.0, 13.4 and 12.9 wt% by chemical assay for the +212, –212/+106, –106/+25 and –25 µm fractions. Cerium returns 0.20, 0.35, 0.37 and 0.29 wt% against 0.18, 0.34, 0.38 and 0.29 wt%. Both track the assay within a few percent relative across the full size range.

4.3. Apatite Crystal-Chemical Formula (apfu) Calculation

EPMA and LA-ICP-MS analyses of the 100 TIMA-X-preselected grains confirm consistent, substantial REE enrichment (Table 3). Representative BSE images are shown in Figure 2. Average EPMA totals for La_2O_3 + Ce_2O_3 + Nd_2O_3 + Y_2O_3 come to 5.4 wt%, with individual grains reaching 4.08 wt% Ce_2O_3 on their own. LA-ICP-MS resolves the same signal at trace-element level: average Ce 28,683 ppm, La 11,602 ppm, Nd 11,346 ppm and Y 3,023 ppm, placing average whole-grain TREE+Y at 6.2–6.4 wt%. Strontium is also high, averaging 15,565 ppm and reaching 2.38 wt% SrO by EPMA, consistent with the coupled Sr-REE substitution reported for carbonatitic apatite (Chakhmouradian et al., 2017).

Table 3. Minimum, maximum and average fluorapatite chemistry from EPMA (oxide wt%) and LA-ICP-MS (ppm) of selected elements, n = 100 grains.

Method	Oxide / element	Min	Max	Avg.
EPMA (wt%)	CaO	47.59	53.96	49.96
	P2O5	34.25	41.47	37.24
	SiO2	0.33	3.51	2.23
	SrO	1.19	2.38	1.55
	Na2O	0.05	0.23	0.13
	La2O3	0.21	2.3	1.44
	Ce2O3	0.48	4.08	2.72
	Nd2O3	0.17	1.46	0.95
	Y2O3	0.04	0.43	0.27
	F	2.54	4.48	3.48
	Cl	0	0.04	0.02
	Total	97.33	100.86	98.64
LA-ICP-MS (ppm)	La	2,026	18,799	11,602
	Ce	5,204	43,273	28,683
	Pr	603	5,115	3,212
	Nd	2,074	18,403	11,346
	Sm	287	2,488	1,534
	Eu	58	554	350
	Gd	188	1,606	1,022
	Dy	97	1,059	619
	Y	400	4,945	3,023
	Sr	10,610	24,731	15,565
	Th	65	5,470	1,462
	U	0.3	226	76

EPMA cannot measure H_2O, which is needed to calculate structural OH, and F is prone to migration under the beam. Normalizing apatite analyses to oxygen therefore introduces systematic error. Following standard practice for the apatite supergroup, formulae were calculated instead by normalizing to 8 total cations (A-site plus X-site, halogens excluded), consistent with the general formula $A_5(XO_4)_3Z$. The A-site (ideal sum 5) takes Ca, Sr, Na, Y

and REE, with minor Fe, Mn and Mg; the X-site (ideal sum 3) takes P, Si and S; the Z-site (ideal sum 1) takes F, Cl and OH (Pan & Fleet, 2002). Oxide weight percentages were converted to molar proportions and scaled so that A- plus X-site cations sum to exactly 8.000.

Normalizing the average composition to 8 total cations gives the formula $(Ca_{4.73}REE_{0.18}Sr_{0.08}Na_{0.02})\Sigma_{5.01}(P_{2.79}Si_{0.20})\Sigma_{2.98}O_{12}(F_{0.97}OH_{0.03})$. The A-site totals 5.017 apfu against an ideal 5.000, with REE+Y (La + Ce + Nd + Y = 0.178 apfu) and Sr (0.079 apfu) taking the place of Ca (4.729 apfu). The X-site totals 2.982 apfu against an ideal 3.000, with Si at 0.197 apfu offsetting a matching P deficiency. That pairing is diagnostic: it is the coupled $REE^{3+} + Si^{4+} \leftrightarrow Ca^{2+} + P^{5+}$ exchange, the britholite component, identified as the dominant REE-accommodation mechanism in carbonatitic and other igneous apatite (Pan & Fleet, 2002; Mao et al., 2016; Anenburg et al., 2021). The Z-site carries 0.975 apfu of measured F plus Cl, leaving 0.025 apfu attributable to unmeasured structural OH.

The average formula for H-K apatite is therefore that of a near end-member fluorapatite, not a hydroxylapatite or chlorapatite. The stoichiometry closes without invoking any additional REE-bearing phase, which means the measured whole-grain REE budget sits inside the apatite structure rather than in sub-micron inclusions. The REE are dispersed through that structure at roughly one cation in every 28 A-site positions; the implications for comminution are developed below.

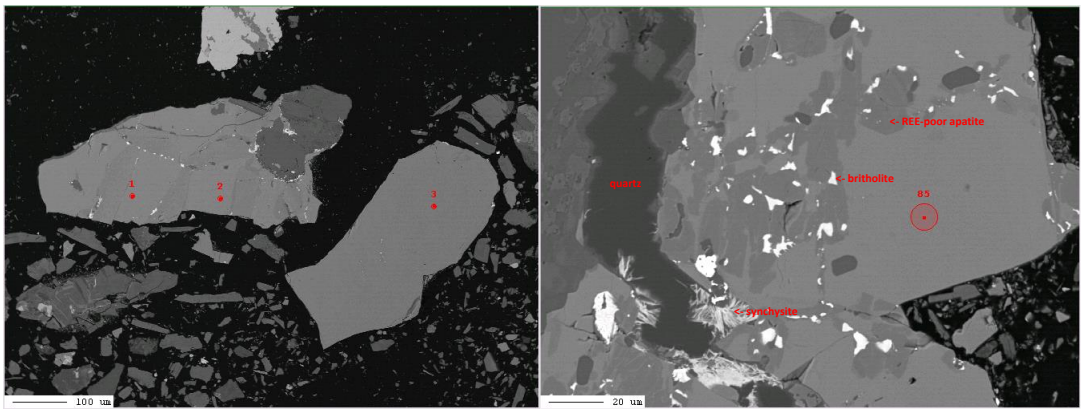

Figure 2. Representative back-scattered electron images of analyzed fluorapatite grains, showing EPMA and LA-ICP-MS spot locations.

4.4. REE Deportment

REE deportment was calculated by combining the mineral masses measured by TIMA-X with the measured mineral chemistry. In the Composite, the calculated Ce and La deportment (Figure 3) shows that apatite hosts 80.6% of the Ce and 87.4% of the La. Deportment in the eight variability samples confirms fluorapatite as the dominant REE host deposit-wide, with its share varying according to local REM abundance. Fluorapatite carries 51.9–96.2% of the Ce mass and 65.4–98.2% of the La mass. In six of the eight samples it accounts for more than 85% of both elements. Sample E446142 is the clear outlier: there, monazite, synchysite and bastnasite between them take about 48% of the

Ce and 34% of the La, reflecting a locally elevated discrete-REM content in that intercept. Sample D141577 is intermediate, with fluorapatite at 78.8% of Ce and 85.9% of La.

The pattern is consistent with the Composite result. Fluorapatite is a moderate modal phase but the principal REE carrier, and the discrete REM only become quantitatively relevant where their abundance rises well above the deposit average.

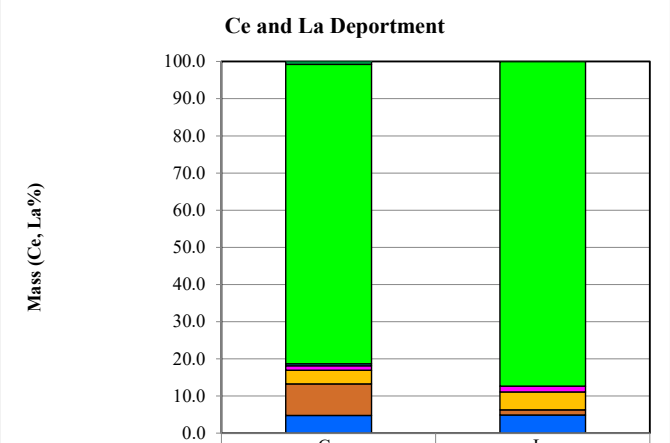

	Ce	La
Apatite/Silicates	0.7	0.0
Apatite	80.6	87.4
Zr Silicates	0.5	0.0
Pyrochlore/Columbite	1.2	1.6
Other REM	3.7	4.8
Synchysite/Bastnasite	8.5	1.4
Monazite	4.8	4.9

Figure 3. Ce and La deportment calculated for the Composite head sample.

4.5. Grain Size, Liberation and Grade-Recovery

Fluorapatite is coarser and better liberated than any of the discrete REM (Table 4, Figure 4). At the Composite P_{80} of 183 µm, fluorapatite liberation, counting pure, free and liberated grains, reaches 84.1% overall. It rises from 44.8% in the +212 µm fraction to 91.8% in the –25 µm fraction. Discrete REM liberation is much lower: 26.8% for monazite, 49.5% for synchysite and bastnasite, and 25.4% for pyrochlore and columbite. Most of what liberation they do achieve comes from the –25 µm fraction, where they increasingly report as slimes.

Grade-recovery curves modeled from TIMA-X particle data reinforce the point. A fluorapatite concentrate above 90% grade is achievable at better than 90% apatite recovery from the three finer fractions. The coarse (+212 µm) fraction tops out near 80% grade at 80% recovery and falls away steeply beyond that. A target grind finer than roughly 212 µm is therefore a design requirement, not an optimization.

Table 4. Grain size and combined liberation of fluorapatite and the discrete REE minerals, Composite sample.

Phase	Median grain size (µm)	P80 grain size (µm)	Liberation, combined (mass%)
Monazite	11	21	26.8
Synchysite / Bastnasite	3	5	49.5
Pyrochlore / Columbite	16	44	25.4
Apatite	53	117	84.1
Particle	63	183	–

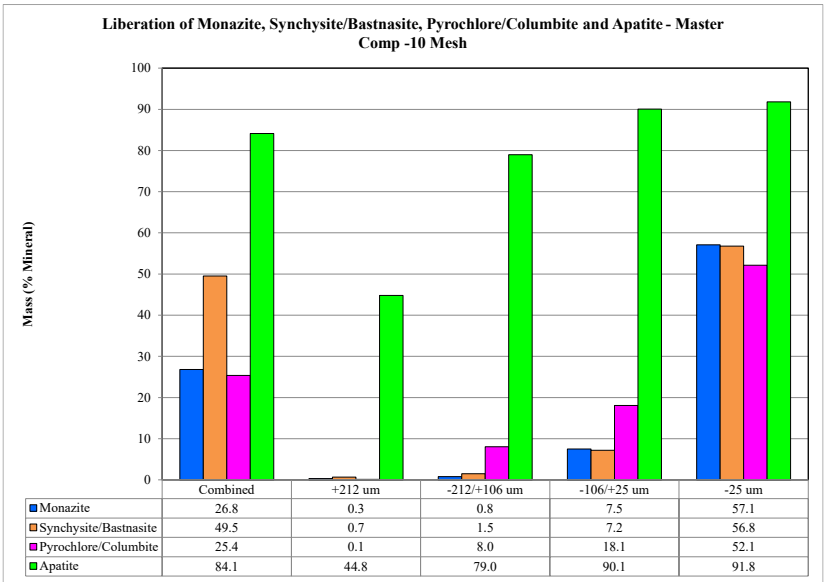

	Combined	+212 um	-212/+106 um	-106/+25 um	-25 um
Monazite	26.8	0.3	0.8	7.5	57.1
Synchysite/Bastnasite	49.5	0.7	1.5	7.2	56.8
Pyrochlore/Columbite	25.4	0.1	8.0	18.1	52.1
Apatite	84.1	44.8	79.0	90.1	91.8

Figure 4. Liberation of the discrete REE minerals and of fluorapatite by size fraction, Composite sample.

4.6. Variability Samples

The eight variability samples span a much wider compositional range than the Composite, as expected given their broader spatial distribution. Fluorapatite ranges from 28.02 to 56.25 wt%, averaging 42.27 wt%, roughly 2.5 to 5 times the Composite grade. Magnetite (2.75–34.22 wt%) and pyroxene (1.57–25.53 wt%) show the widest relative variations among the gangue phases. Discrete REM stay minor throughout: monazite reaches 0.89 wt%, synchysite runs 0.35–2.02 wt%, pyrochlore reaches 0.97 wt%. The fluorapatite-hosted REE association is a deposit-wide feature, not an artifact of compositing.

Liberation behavior holds up across the suite as well. Fluorapatite liberation ranges 80–92%, consistently above monazite (17–68%, the best-liberated of the REM group). Fluorapatite P_{80} grain size runs 49–253 µm against 10–24 µm for monazite and 8–19 µm for synchysite and bastnasite, roughly an order of magnitude coarser. The processing strategy derived from the Composite is transferable to the full range of ore sampled.

5. Discussion

5.1. Fluorapatite, Not Discrete REM, as the Processing Target

The results indicate that the discrete REM are too scarce (0.58 wt% of the Composite), too fine (median 3–16 μm) and too poorly liberated (25.4–49.5%) to support a conventional REM concentrate. Even in the finest fraction their liberation stays below 57%. Grinding finer to improve on that would be difficult to justify against an inventory that represents well under 1 wt% of the feed mass. Fluorapatite is the opposite case on every count. It is the dominant REE host (52–98% of Ce and La across the suite), it is the better-liberated phase (84.1% at 183 μm), and it is coarse enough that a conventional grind reaches it. Apatite hosts the majority of the REE+Y and is therefore the principal REE target.

This is why the metallurgical objective inverts. The task is not to concentrate REE minerals; it is to concentrate fluorapatite, and then to leach it. The same logic has been demonstrated on other iron-rich fluorapatite concentrates, notably at Esfordi, Iran, where selective leaching of Ca and phosphate followed by acid baking of the residue recovers both the phosphate and the contained REE (Soltani et al., 2019).

5.2. From Mineralogy to Flowsheet

Given the fact that the REE are lattice-bound, physical beneficiation can only ever deliver a fluorapatite concentrate; the REE grade of that concentrate is fixed by the apatite chemistry, at 6.2–6.4 wt% TREE+Y, and cannot be improved by further physical separation. These grades do not include any additional contributions from REM associated with apatite. The mineralogy sets the concentrate grade and the circuit only determines recovery.

Thus, flowsheet development could be discussed around three aspects: (1) how efficiently can fluorapatite be recovered; (2) how much gangue, particularly iron, could be associated with the apatite; and (3) how readily does the phosphate lattice give up its REE in leach. On the first, the liberation and grade-recovery data support flotation of a high-grade apatite concentrate at a grind finer than 212 μm. On the second, the 6.5–13 wt% magnetite content (Composite to variability average) makes magnetic separation ahead of the leach circuit a straightforward way to reject iron oxide and reduce acid consumption downstream. On the third, preliminary testwork reported alongside this dataset indicates better than 75% TREO recovery by direct acid leach of fluorapatite concentrate at approximately 50°C over roughly 6 hours, a much simpler operation than conventional REM cracking.

The resulting intermediate is a REE-enriched phosphate, a product that existing infrastructure is already equipped to handle. REE can be co-recovered as a byproduct of purified phosphoric acid manufacture, and the confirmed enrichment of other elements (e.g., gallium) in the fluorapatite fraction (up to 55 ppm) adds a further co-product relevant to semiconductor and defence supply chains. Magnetite is a saleable co-product in its own right, and the columbite-group minerals warrant further metallurgical work.

5.3. Regional and Global Context

Benchmarked against other REE-enriched apatite occurrences, H-K fluorapatite (5.9 wt% TREE; 6.2–6.4 wt% TREE+Y) is well above typical carbonatite apatite, which accommodates REE, Sr, Na, Mn and Th across a wide but generally sub-percent range (Pan & Fleet, 2002; Mao et al., 2016). It also compares favourably with several occurrences already considered economically significant. In the Kola Alkaline Province, apatite reaches 4,400 ppm REE at Kovdor, and 3.5–5.2 wt% REE_2O_3 in late-stage Khibina carbonatite rocks (Zaitsev et al., 2014). At the Khibiny apatite-nepheline deposits, mined for phosphate for close to a century and now treated as a world-class REE-in-apatite resource, apatite averages 4.5 wt% SrO with REE up to 8,891 ppm (Kogarko, 2018). At Nolans Bore, Northern Territory, REE-P-Th mineralization is likewise carried almost entirely in fluorapatite veins, supporting a JORC resource of 56 Mt at 2.6% TREO (Huston et al., 2016; Anenburg et al., 2020a).

H-K fluorapatite sits above the Kola and Nolans Bore (Zaitsev et al., 2014) ranges and approaches the most REE-rich natural apatite known, from the Ilímaussaq complex in Greenland (Zirner et al 2015; Rønsbo, 2008), where individual grains are up to 27 wt% REE_2O_3 through the same britholite substitution documented here. The comparison places H-K fluorapatite toward the high-grade end of the global range, alongside occurrences that already support or are advancing toward production.

The petrological context is consistent with that outcome. Experimental work on carbonatite REE mobilization shows that silica-saturated conditions drive REE into early-crystallizing fluorapatite by way of the britholite substitution, rather than leaving them available to late-stage, more soluble REE-carbonate phases (Anenburg et al., 2020b; Anenburg et al., 2021). The silicate-dominated biotite-amphibole-pyroxene assemblage enclosing H-K fluorapatite, together with the low discrete-REM inventory, is what that model predicts. The H-K is characterized by high apatite REE tenor, coarse and well-liberated apatite, and a location at surface with road and hydroelectric power already in place.

6. Conclusions

Integrated XRD, TIMA-X, EPMA and LA-ICP-MS characterization of the Hecla-Kilmer deposit supports six findings.

- Discrete REE minerals total 0.58 wt% of the Composite and remain minor across all eight variability samples. This is roughly an order of magnitude too little to carry the measured whole-rock grades of 4,258–8,093 g/t TREE+Y.
- Fluorapatite is the primary REE host at deposit scale. It comprises 11.3 wt% of the Composite by TIMA-X and 28.0–56.3 wt% across the variability samples, carries 5.9 wt% TREE and 6.2–6.4 wt% TREE+Y, and hosts 52–98% of the Ce and La mass.
- Normalization of average EPMA data to 8 cations gives $(Ca_{4.73}REE_{0.18}Sr_{0.08}Na_{0.02})\Sigma_{5.01}(P_{2.79}Si_{0.20})\Sigma_{2.98}O_{12}(F_{0.97}OH_{0.03})$, confirming a coupled $REE^{3+}+Si^{4+} \leftrightarrow Ca^{2+}+P^{5+}$ substitution in a near end-member fluorapatite. At roughly one REE cation per 28 A-sites, the REE cannot be liberated by comminution at any grind size.

- Fluorapatite liberation reaches 84.1% at a P_{80} of 183 µm, against 25.4–49.5% for the discrete REM. Grade-recovery modeling supports a concentrate above 90% grade at better than 90% recovery from material finer than approximately 212 µm.
- Together these results move the H-K processing strategy away from discrete REM concentration and toward a high-grade, REE-enriched fluorapatite concentrate for direct leaching, with co-recovery of REE, gallium and phosphate within existing phosphoric acid infrastructure and magnetite as an additional product. The mineralogy fixes the achievable concentrate grade; the circuit determines recovery. That distinction should be settled before flowsheet development begins on any apatite-hosted REE deposit.
- The testwork illustrates a general point: for REE as for other metals, grade alone does not guarantee recovery unless the mineralogy is understood and the flowsheet is adapted accordingly.

Acknowledgments

The authors acknowledge financial support from the Government of Ontario through the Ontario Junior Exploration Program (OJEP), which contributed over $600,000 toward exploration at the Hecla-Kilmer project, including drill core sampling, and from the Government of Canada through Natural Resources Canada's Critical Minerals Innovation Fund (CMIF), which contributed $500,000 toward metallurgical and processing testwork. Mineralogical and metallurgical analytical work was carried out at SGS Canada Inc., Lakefield, Ontario. Hydrometallurgical process scoping is being conducted by Dorfner Anzaplan GmbH, whose contribution is gratefully recognized. We thank the reviewers and editors for comments that improved the manuscript.

References

Anenburg, M., Mavrogenes, J.A. & Bennett, V.C. (2020a) The fluorapatite P–REE–Th vein deposit at Nolans Bore: genesis by carbonatite metasomatism. Journal of Petrology, Vol. 61, No. 1: egaa003

Anenburg, M., Mavrogenes, J.A., Frigo, C. & Wall, F. (2020b) Rare earth element mobility in and around carbonatites controlled by sodium, potassium, and silica. Science Advances 6(41), eabb6570

Anenburg, M., Broom-Fendley, S. & Chen, W. (2021) Formation of rare earth deposits in carbonatites. Elements 17(5), 327–332.

Broom-Fendley, S., Styles, M.T., Appleton, J.D., Gunn, G. & Wall, F. (2016) Evidence for dissolution-reprecipitation of apatite and preferential LREE mobility in carbonatite-derived late-stage hydrothermal processes. American Mineralogist 101(3), 596–611.

Chakhmouradian, A.R., Reguir, E.P., Zaitsev, A.N., Couëslan, C., Xu, C., Kynický, J., Mumin, A.H. & Yang, P. (2017) Apatite in carbonatitic rocks: compositional variation, zoning, element partitioning and petrogenetic significance. Lithos, 274–275, 188–213.

Fandrich, R., Gu, Y., Burrows, D. & Moeller, K. (2007) Modern SEM-based mineral liberation analysis. International Journal of Mineral Processing 84(1–4), 310–320.

Grammatikopoulos, T. (2026) An investigation into the mineralogical examination of one composite and eight variability samples from the Hecla-Kilmer deposit, Northern Ontario. Report CALR-19602-01 / MI5013-AUG23, prepared for Neotech Metals Corp., 120 pp.

Gugala, E. (2025) Unlocking value through process mineralogy: TIMA-powered automated characterization of raw materials. Presented at PTMin 2025, TESCAN.

Huston, D.L., Maas, R., Cross, A., Hussey, K.J., Mernagh, T.P., Fraser, G. & Champion, D.C. (2016) The Nolans Bore rare earth element–phosphorus–uranium mineral system: geology, origin and post-depositional modifications. Mineralium Deposita 51, 797-822.

Kato, Y., Fujinaga, K., Nakamura, K., Takaya, Y., Kitamura, K., Ohta, J., Toda, R., Nakashima, T. & Iwamori, H. (2011) Deep-sea mud in the Pacific Ocean as a potential resource for rare-earth elements. Nature Geoscience 4(8), pp. 535-539.

Kogarko, L.N. (2018) Chemical composition and petrogenetic implications of apatite in the Khibiny apatite-nepheline deposits (Kola Peninsula). Minerals 8(11), 532.

Mao, M., Rukhlov, A.S., Rowins, S.M., Spence, J. & Coogan, L.A. (2016) Apatite trace element compositions: a robust new tool for mineral exploration. Economic Geology 111(5), pp. 1187–1222.

Özer, M., Gümüş, G., Unluer, A.T., Doner, Z., Özdamar, Ş., Kökkılıç, O. & Burat, F. (2025) Characterization and Enrichment of Rare Earth Element and Heavy Mineral-Bearing Fractions from the Hantepe Placer Deposit, Çanakkale, Türkiye. Minerals, Vol. 15, 1293.

Pan, Y. & Fleet, M.E. (2002) Compositions of the apatite-group minerals: substitution mechanisms and controlling factors. Reviews in Mineralogy and Geochemistry 48(1), pp. 13-49.

Rønsbo, J.G. (2008) Apatite in the Ilímaussaq alkaline complex: Occurrence, zonation and compositional variation. Lithos 106(1-2), pp. 71-82.

Soltani, F., Abdollahy, M., Petersen, J., Ram, R., Koleini, S.M.J. & Moradkhani, D. (2019) Leaching and recovery of phosphate and rare earth elements from an iron-rich fluorapatite concentrate. Part II: selective leaching of calcium and phosphate and acid baking of the residue. Hydrometallurgy, Vol 184, pp. 29–38.

Sylvester, P.J. (2012) Use of the mineral liberation analyzer (MLA) for mineralogical studies of sediments and sedimentary rocks. Mineralogical Association of Canada Short Course 42, pp. 1–16.

Takaya, Y., Yasukawa, K., Kawasaki, T., Fujinaga, K., Ohta, J., Usui, Y., Nakamura, K., Kimura, J., Chang, Q., Hamada, M., Dodbiba, G., Nozaki, T., Iijima, K., Morisawa, T., Kuwahara, T., Ishida, Y., Ichimura, T., Kitazume, M., Fujita, T. & Kato, Y. (2018) The tremendous potential of deep-sea mud as a source of rare-earth elements. Scientific Reports 8(1), 5763.

Zirner, A.L.K., Mark, M.A.W., Wenzel, T., Jacob, D.E. & Markl, G. (2015) Rare earth elements in apatite as a monitor of magmatic and metasomatic processes: the Ilímaussaq complex, South Greenland. Lithos 228-229, pp. 12-22.

Zaitsev, A.N., Williams, C.T., Jeffries, T.E., Strekopytov, S., Moutte, J., Ivashchenkova, O.V., Spratt, J., Petrov, S.V., Wall, F., Seltmann, R. & Borozdin, A.P. (2014) Rare earth elements in phoscorites and carbonatites of the Devonian Kola Alkaline Province, Russia: examples from Kovdor, Khibina, Vuoriyarvi and Turiy Mys complexes. Ore Geology Reviews 61, 204-225.

Xu, C., Chi, R., Zhang, Y., Zhong, C., Ruan, Y., Lyu, R. & Zhou, F. (2020) Process mineralogy of Bayan Obo rare earth ore by MLA. Physicochemical Problems of Mineral Processing, Vol. 56, Issue 4. pp. 737-745

Watts, K.E. & Andersen, A.K. (2025) Complex carbonate ore mineralogy in the Mountain Pass carbonatite rare earth element deposit, USA. American Mineralogist, Vol. 111, Issue 1, pp. 11–28.